Geophys. J. Int. (2010) **181,** 493–501 doi: 10.1111/j.1365-246X.2010.04515.x

Resolving fault plane ambiguity for small earthquakes

Po Chen,[1] Thomas H. Jordan[2] and Li Zhao[3]

[1] *Department of Geology and Geophysics, University of Wyoming, USA. E-mail: pchen@uwyo.edu*
[2] *Department of Earth Sciences, University of Southern California, USA*
[3] *Institute of Earth Sciences, Academia Sinica, Taiwan*

Accepted 2010 January 8. Received 2010 January 4; in original form 2009 November 13

SUMMARY

We have developed an automated procedure to resolve fault-plane ambiguity for small to medium-sized earthquakes ($2.5 \leq M_L \leq 5$) using synthetic Green's tensors computed in a 3-D earth structure model and applied this procedure to 35 earthquakes in the Los Angeles area. For 69 per cent of the events, we resolved fault plane ambiguity of our CMT solutions at 70 per cent or higher probability. For some earthquakes, the fault planes selected by our automated procedure were confirmed by the distributions of relocated aftershock hypocentres. In regions where there are no precisely relocated aftershocks or for earthquakes with few aftershocks, we expect our method to provide the most convenient means for resolving fault plane ambiguity. Our procedure does not rely on detecting directivity effects; therefore it is applicable to any types of earthquakes.

Key words: Earthquake source observations; Seismicity and tectonics; Computational seismology.

INTRODUCTION

A fundamental ambiguity of the most general point-source representation of an earthquake, the centroid moment tensor (CMT), is that it does not specify which of the two nodal planes is the actual fault plane (Aki & Richards 2002). To identify the fault plane, additional information about the seismic source is needed.

The lowest-order representation of a finite rupture is the finite moment tensor (FMT, Chen *et al.* 2005), which contains the second-order polynomial moments of the source–space–time function in addition to the zeroth- and first-order polynomial moments included in the CMT parameters (Backus & Mulcahy 1976; McGuire *et al.* 2001). The FMT representation resolves fault-plane ambiguity from the CMT representation and gives the characteristic duration (Silver & Jordan 1983) and dimensions of the faulting as well as the directivity vector of the fault slip (Ben-Menahem 1961).

In previous studies that derive finite source properties for small to medium-sized earthquakes, empirical Green's functions (EGF) were often employed to account for propagation path-effects (Mori 1996; Hellweg & Boatwright 1999; McGuire 2004). In Chen *et al.* (2005) we demonstrated the feasibility of full FMT inversion for regional medium-sized earthquakes ($4.5 \leq M_L \leq 6$) using high-frequency ($\sim$2.5 Hz) waveform data. We corrected the propagation path-effects in the observed data using synthetic Green's functions computed in path-averaged 1-D Earth structure models and a 'denuisancing' technique, which is similar to, but more flexible than traditional EGF techniques.

With the advancement of computing technology and numerical methods, synthetic Green's functions can be calculated accurately in 3-D Earth structure models using finite-difference (FD, Olsen 1994; Graves 1996; Olsen *et al.* 2003), finite-element (Bao *et al.* 1998; Akcelik *et al.* 2003) and spectral-element methods (Komatitsch *et al.* 2004). In regions such as Southern California, preliminary 3-D Earth structure models are already available (Magistrale *et al.* 2000; Kohler *et al.* 2003; Süss & Shaw 2003), and efficient numerical methods have been adapted to simulate seismic wave propagation in these 3-D Earth structure models (Komatitsch *et al.* 2004; Olsen *et al.* 2006). Our automated procedure for CMT inversion and fault-plane ambiguity resolution is built upon these previous achievements. In this paper, we demonstrate the feasibility of resolving fault-plane ambiguity for local small to medium-sized earthquakes ($2.5 \leq M_L \leq 5$) using FD synthetic Green's functions computed in a 3-D structural model, the Southern California Earthquake Center (SCEC) Community Velocity Model Version 3.0 (CVM3.0). For most local small events, the low-frequency data ($<$1 Hz) that can be accurately modeled by FD synthetic Green's functions are usually insufficient for precise determination of all FMT parameters. However, we show that the low-frequency data can be used to detect the constructive/destructive interference effects caused by the second-order spatial moment and to establish the probability that one of the CMT nodal planes is the actual fault plane. This technique does not rely on detecting directivity effects therefore it is applicable to any type of seismic source, including bilateral earthquakes with no directivity.

FORMULATION

Receiver Green's tensor (RGT)

Our procedure relies on the use of receiver Green's tensors (RGTs) $G_{ik}(\mathbf{r}, \mathbf{r}_R; t)$ and seismic reciprocity principle (Aki & Richards 2002). The RGT G_{ik} is the ith component wavefield at position $\mathbf{r}$ and time t for a kth component impulsive point-force at the receiver position $\mathbf{r}_R$ (Zhao *et al.* 2005). Seismic reciprocity implies that the synthetic seismogram at $\mathbf{r}_R$ excited by a point source with moment tensor M_{ij} at position $\mathbf{r}_S$ at time t_S is

$$\tilde{u}_k(t) = \sum_{ij} M_{ij} \partial_j^S G_{ki}(\mathbf{r}_R, \mathbf{r}_S; t - t_S) = \sum_{ij} M_{ij} \partial_j^S G_{ik}(\mathbf{r}_S, \mathbf{r}_R; t - t_S), \quad (1)$$

where ∂^S denotes source-coordinate gradient with respect to $\mathbf{r}_S$. We calculated G_{ik} for 48 broad-band stations of the California Integrated Seismic Network (CISN) in the Los Angeles region (Fig. 1) using the SCEC CVM3.0 (Magistrale *et al.* 2000; Kohler *et al.* 2003), and the fourth-order staggered-grid finite-difference code (Olsen 1994). These receiver Green's tensors were sampled on a regular mesh of 36 million gridpoints with a grid-spacing of 200 m and archived on a RAID storage system at the High-performance Computing Center in University of Southern California, where they occupied a total data volume of about 20 TB (TB $= 10^{12}$ bytes). Point-source synthetic seismograms were calculated by retrieving G_{ik} on a small source-centred grid and calculating the source-coordinate gradient ∂_j^S using a fourth-order numerical differentiation scheme (Press *et al.* 1992). Details about the construction of our RGT database as well as our automated CMT inversion procedure are documented in a separate paper (Zhao *et al.* 2006).

Generalized seismological data functional (GSDF)

The waveform differences between observed seismograms and point-source synthetics generated from a CMT solution and the RGTs by applying the reciprocity principle (eq. 1) can be parametrized using the generalized seismological data functionals (GSDF) of Gee & Jordan (1992). In the frequency domain, we can map the synthetic waveform

$$\tilde{u}_k(\omega) = \exp\{\mathrm{i}\omega[\tilde{\tau}_p(\omega) + \mathrm{i}\tilde{\tau}_q(\omega)]\} \quad (2)$$

into the observed waveform using two frequency-dependent, time-like quantities $\delta\tau_p(\omega)$ and $\delta\tau_q(\omega)$

$$u_k(\omega) = \tilde{u}_k(\omega) \exp\{\mathrm{i}\omega[\delta\tau_p(\omega) + \mathrm{i}\delta\tau_q(\omega)]\}. \quad (3)$$

In GSDF analysis, we estimate $\delta\tau_{p,q}(\omega)$ by measuring frequency-dependent phase-delay time $\delta t_p(\omega_n)$ and amplitude-reduction time $\delta t_q(\omega_n)$ at a set of discrete frequencies ω_n. The measured $\delta t_x(\omega_n)$ (x = p, q) are weighted averages of $\delta\tau_x(\omega_n)$ in narrow frequency bands centred around ω_n (Chen 2005; Chen *et al.* 2007a). The phase-delay time δt_p is the frequency-dependent generalization of differential travel time and the amplitude-reduction time δt_q is the frequency-dependent generalization of differential t^*.

Finite moment tensor (FMT)

Any indigenous seismic source can be represented using a space–time distribution of stress glut $\Gamma(\mathbf{r}, t)$ (Backus & Mulcahy 1976). If we assume the stress glut is everywhere proportional to

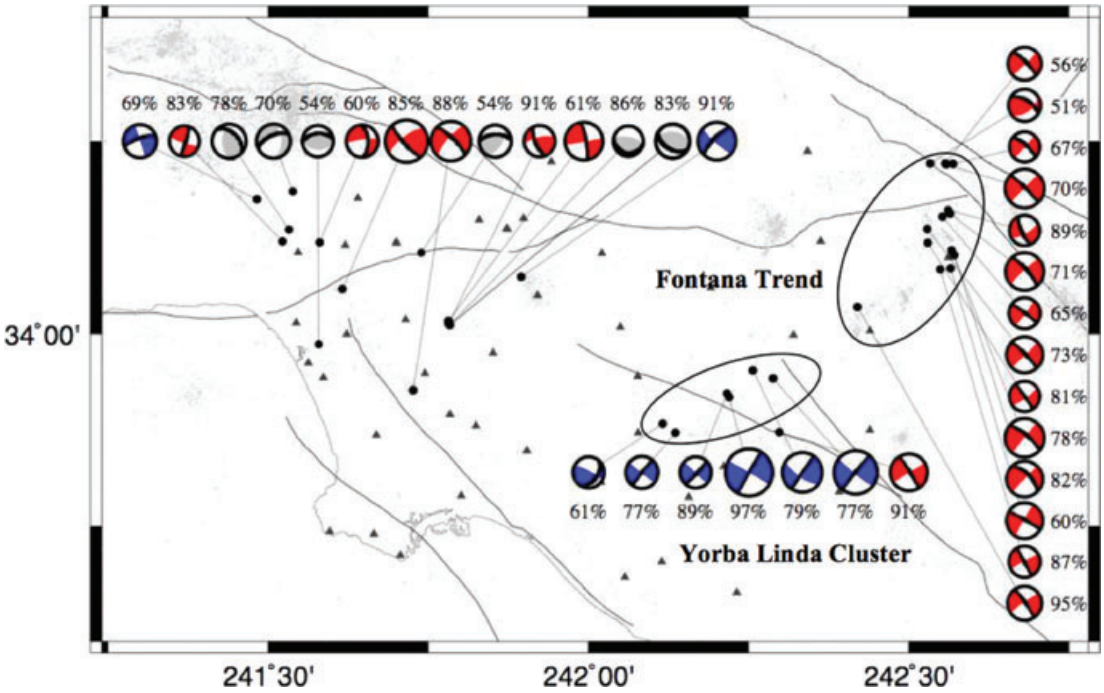

Figure 1. Focal mechanisms with fault-plane ambiguity resolutions for 35 small to medium-sized earthquakes in the Los Angeles area. The preferred fault planes picked by our automated procedure are highlighted in thick black lines. Left-lateral events have blue extensive quadrants; right-lateral events have red extensive quadrants. The numbers near the beachballs indicate the likelihood that the preferred nodal planes are the actual fault planes based on a bootstrap procedure (see text). Epicentres of these 35 earthquakes are indicated by the black dots. Background seismicity in this area is shown in grey points. CISN stations used in this study are shown as grey triangles. Major faults in this area are plotted as black solid lines. The two seismicity anomalies discussed in the text, the Yorba Linda cluster and the Fontana trend, are indicated with the two black ellipses.

a constant seismic moment tensor, $\Gamma(\mathbf{r}, t) = \mathbf{M}\int_{t_0}^{t} f(\mathbf{r}, t')\mathrm{d}t'$, the seismic wavefield is proportional to the source space–time function $f(\mathbf{r},t)$, which we expand in terms of its space–time polynomial moments $\mu^{(m,l)}$. Here, m and l represent the order of spatial and temporal moments. The zeroth-order moment is by definition unity, $\mu^{(0,0)} = \iint f(\mathbf{r}, t)\mathrm{d}V\mathrm{d}t = 1$, and the first moments yield the source centroid:

$$\boldsymbol{\mu}^{(1,0)} = \iint f(\mathbf{r}, t)\mathbf{r}\mathrm{d}V\mathrm{d}t \equiv \mathbf{r}_1, \quad \mu^{(0,1)} = \iint f(\mathbf{r}, t)t\mathrm{d}V\mathrm{d}t \equiv t_1. \tag{4}$$

The tensor $\mathbf{M}$, vector $\mathbf{r}_1$, and scalar t_1 form the CMT (point-source) representation. The lowest order description of source finiteness is given by the second moments. The second central moment in time gives the characteristic duration of the event (e.g. Silver & Jordan 1983),

$$\hat{\mu}^{(0,2)} = \iint f(\mathbf{r}, t)(t - t_1)^2\mathrm{d}V\mathrm{d}t \equiv (T_\mathrm{C}/2)^2. \tag{5}$$

The second central moment in space is a symmetric second-order tensor

$$\hat{\boldsymbol{\mu}}^{(2,0)} = \iint f(\mathbf{r}, t)(\mathbf{r} - \mathbf{r}_1)(\mathbf{r} - \mathbf{r}_1)^\mathrm{T}\mathrm{d}V\mathrm{d}t = \mathbf{U}\Lambda\mathbf{U}^\mathrm{T}. \tag{6}$$

Here Λ is a diagonal matrix of eigenvalues, and $\mathbf{U}$ is an orthogonal matrix of eigenvectors. For the special case of a planar rectangular dislocation of length L and width W, the two non-zero eigenvalues will be $(L_\mathrm{C}/2)^2$ and $(W_\mathrm{C}/2)^2$, where $L_\mathrm{C} = L/3$ is the characteristic length and $W_\mathrm{C} = W/3$ is the characteristic width of the source. For the 2002 September 3 M_L 4.8 Yorba Linda earthquake investigated in Chen *et al.* (2005), the second central moment in space is given by

$$\Lambda = \mathrm{diag}\left[\left(\frac{0.74}{2}\right)^2, \left(\frac{0.4}{2}\right)^2, 0\right],$$

$$\mathbf{U} = \begin{bmatrix} \cos(-20^\circ)\cos(30^\circ) & \cos(-110^\circ)\cos(30^\circ) & \sin(30^\circ) \\ \cos(-20^\circ)\sin(30^\circ) & \cos(-110^\circ)\sin(30^\circ) & -\cos(30^\circ) \\ \sin(-20^\circ) & \sin(-110^\circ) & 0 \end{bmatrix},$$

where diag[ ] denotes a diagonal matrix, the planar rupture has a characteristic length of 0.74 km, width 0.4 km and the first principle axis has a strike of 30° and tilts 20° upwards (x-north, y-east and z-down). The mixed space–time moment yields the directivity vector (Ben-Menahem 1961; McGuire *et al.* 2001),

$$\hat{\boldsymbol{\mu}}^{(1,1)} = \iint f(\mathbf{r}, t)(\mathbf{r} - \mathbf{r}_1)(t - t_1)dVdt \equiv \mathbf{v}_\mathrm{d} \cdot \hat{\mu}^{(0,2)}. \tag{7}$$

The directivity velocity vector $\mathbf{v}_\mathrm{d}$ will lie in the plane of a simple dislocation. For a perfect bilateral rupture, the directivity parameter $D \equiv |\mathbf{v}_\mathrm{d}|\ T_\mathrm{C}/L_\mathrm{C}$ will be zero, and for a perfect unilateral rupture, it will be unity. In previous studies, McGuire *et al.* (2002) inverted low-frequency teleseismic waveform data for FMT parameters and showed that global large earthquakes ($M_\mathrm{w} \geq 7.0$) are predominantly unilateral. McGuire (2004) and Chen *et al.* (2005) inverted broad-band waveform data for FMT parameters of local medium-sized earthquakes ($4.0 \leq M_\mathrm{w} \leq 5.0$) and showed that the symmetry breaking process also happens at a much smaller scale.

In general, the FMT representation will comprise the 10 parameters of the CMT plus 10 additional parameters that specify the second central moments of $f(\mathbf{r},t)$. In the analysis of small earthquakes described below, we have generally assumed a planar dislocation (double-couple) source, which reduces the number of CMT parameters to 8 and the total number for the FMT to 13.

The partial derivatives of $\tilde{\tau}_\mathrm{x}(\omega)$ with respect to FMT parameters $\boldsymbol{\mu}^{(m,l)}$ ($m+l \leq 2$) have been derived in McGuire *et al.* (2001). The linearized forward problem that relates the perturbation $\delta\tilde{\tau}_\mathrm{x}(\omega)$ to $\boldsymbol{\mu}^{(m,l)}$ can be expressed as

$$\delta\tilde{\tau}_\mathrm{q}(\mathbf{r}_\mathrm{R}, \omega) \approx \nabla_\mathrm{S}\tilde{\tau}_\mathrm{q} \cdot \boldsymbol{\mu}^{(1,0)} + \frac{\omega}{2}\mu^{(0,2)} + \omega\nabla_\mathrm{S}\tilde{\tau}_\mathrm{p} \cdot \boldsymbol{\mu}^{(1,1)} + \frac{1}{2}\tilde{\mathbf{X}} : \boldsymbol{\mu}^{(2,0)}, \tag{8a}$$

$$\delta\tilde{\tau}_\mathrm{p}(\mathbf{r}_\mathrm{R}, \omega) \approx \mu^{(0,1)} + \nabla_\mathrm{S}\tilde{\tau}_\mathrm{p} \cdot \boldsymbol{\mu}^{(1,0)} + \omega\nabla_\mathrm{S}\tilde{\tau}_\mathrm{q} \cdot \boldsymbol{\mu}^{(1,1)} + \frac{1}{2}\tilde{\mathbf{Y}} : \boldsymbol{\mu}^{(2,0)}. \tag{8b}$$

Here, ∇_S is the gradient operator with respect to source coordinate $\mathbf{r}_\mathrm{S}$, which is approximated by finite-differencing in our automated procedure, and the contributions from the second-order spatial moment $\boldsymbol{\mu}^{(2,0)}$ are proportional to the second-order spatial gradients

$$\tilde{\mathbf{X}} = \nabla_\mathrm{S}\nabla_\mathrm{S}\tilde{\tau}_\mathrm{q} + \omega\nabla_\mathrm{S}\tilde{\tau}_\mathrm{p}\nabla_\mathrm{S}\tilde{\tau}_\mathrm{p} - \omega\nabla_\mathrm{S}\tilde{\tau}_\mathrm{q}\nabla_\mathrm{S}\tilde{\tau}_\mathrm{q}, \tag{9a}$$

$$\tilde{\mathbf{Y}} = \nabla_\mathrm{S}\nabla_\mathrm{S}\tilde{\tau}_\mathrm{p} - \omega\nabla_\mathrm{S}\tilde{\tau}_\mathrm{p}\nabla_\mathrm{S}\tilde{\tau}_\mathrm{q} - \omega\nabla_\mathrm{S}\tilde{\tau}_\mathrm{q}\nabla_\mathrm{S}\tilde{\tau}_\mathrm{p}. \tag{9b}$$

For a finite source with strong directivity, the fault-plane ambiguity can be effectively resolved by examining the azimuthal variation of δt_q at high frequency, which usually has a minimum in the direction of rupture propagation (i.e. a maximum in the amplitude ratio between the observed waveform and the point-source synthetic waveform). This azimuthal variation is mainly due to the contributions from the mixed space–time moment $\boldsymbol{\mu}^{(1,1)}$, whose sensitivity derivative $\omega\nabla_\mathrm{S}\tilde{\tau}_\mathrm{p}$ has a $\cos(\theta)$-dependence on azimuth θ and increases with frequency (McGuire *et al.* 2001; Chen *et al.* 2005).

Resolving fault-plane ambiguity

Most previous studies that resolved fault-plane ambiguity for small to medium-sized earthquakes have relied on detecting directivity effect using empirical Green's function techniques (Mori & Hartzell 1990; Mori 1996; Hellweg & Boatwright 1999; Okada *et al.* 2001; McGuire 2004). For a finite source without significant directivity, it is possible to resolve fault-plane ambiguity by detecting the constructive/destructive interference effect due to source finiteness, which is characterized by the contributions to the waveform from the second-order spatial moment $\boldsymbol{\mu}^{(2,0)}$. In particular, the interference effect due to contributions from $\boldsymbol{\mu}^{(2,0)}$ can be detected by examining the azimuthal and frequency variations of the GSDF measurements. For strike-slip events, the amplitude-reduction time measurements usually have a $\cos(2\theta)$-dependence on azimuth θ with two minima located at 90° and 270° from the strike of the actual fault plane. To demonstrate this point, we give an example in the Appendix.

To resolve fault-plane ambiguity using the contributions from $\boldsymbol{\mu}^{(2,0)}$, we systematically compare the actual GSDF measurements $\delta t_\mathrm{x}(\omega_n)$ with model-predicted measurements $\delta\tilde{t}_\mathrm{x}(\omega_n)$ calculated for the two nodal planes of the CMT solution. The nodal plane that provides better prediction to the actual measurements is picked as the preferred fault plane. To make the GSDF measurements, the observed and point-source synthetic seismograms were first low-pass filtered using a fourth-order Butterworth filter with the corner frequency at 0.5 Hz; GSDF analysis were then applied on selected P, S and surface waves to obtain $\delta t_\mathrm{x}(\omega_n)$ at 0.1, 0.2, 0.3, 0.4 and 0.5 Hz. The model-predicted $\delta\tilde{\tau}_\mathrm{x}(\omega_n)$ were computed using eq. (8) for the two nodal planes of our CMT solution. The model-predicted $\delta\tilde{t}_\mathrm{x}(\omega_n)$ can be obtained by integrating $\delta\tilde{\tau}_\mathrm{x}$ against a seismogram perturbation kernel $I_\mathrm{x}(\omega, \omega_n)$,

$$\delta\tilde{t}_\mathrm{x}(\omega_n) = \int \mathrm{d}\omega I_\mathrm{x}(\omega, \omega_n)\delta\tilde{\tau}_\mathrm{x}(\omega). \tag{10}$$

Event ID	Longitude	Latitude	Depth	Mag	Strike	Dip	Rake	Likelihood	Beachball
14116972	−117.4387	34.125	4.15	4.42	309	80	175	70%	
12663484	−117.8644	33.8721	3.71	3.21	218	89	3	77%	
13692644	−117.4359	34.1562	9.25	3.74	318	77	−173	71%	
14000944	−117.408	34.1672	11.72	3.27	315	82	164	80%	
9020807	−118.5179	34.1749	6.94	3.33	251	74	−1	69%	
9026401	−117.4343	34.1086	4.38	3.87	309	77	−179	78%	
9029821	−117.4295	34.1024	7.62	3.57	314	63	−179	82%	
9038699	−117.7125	33.9425	12.69	4.29	219	88	5	77%	
9039015	−117.8848	33.8835	4.21	3.12	37	43	13	61%	
9039574	−118.4615	34.1849	11.15	3.35	245	61	−47	70%	
9050697	−118.2613	34.1055	8.37	3.16	267	54	131	54%	
9051747	−118.1053	34.074	8.25	3.79	224	74	9	91%	
9055585	−118.478	34.12	9.31	3.02	16	83	169	83%	
9059921	−118.468	34.1355	20.77	3.36	313	45	53	78%	
9072092	−117.4436	34.2214	9.74	3.33	315	79	177	56%	
9077185	−117.4355	34.0855	4.56	3.59	299	86	−175	60%	
9083372	−117.958	33.6661	12.62	3.45	271	60	65	99%	
9089885	−118.2165	34.0118	7.57	3.43	121	50	108	83%	
9089890	−118.2174	34.0119	7.5	3.02	105	24	94	86%	
9092333	−118.2187	34.0139	7.5	3.15	157	68	156	91%	
9093975	−118.2187	34.0172	7.44	3.77	349	80	177	61%	
9097822	−117.4322	34.2206	14.94	3.02	311	77	179	67%	
9115618	−117.4516	34.084	4.59	3.06	151	88	175	87%	
9126312	−118.4201	34.119	4.66	3.21	357	59	−170	60%	
9126657	−117.4478	34.1523	13.71	3.07	306	87	176	65%	
9142023	−117.715	33.811	10.88	3.06	131	51	164	57%	
9142274	−117.4709	34.1184	15.52	3.03	145	89	−168	81%	
9146630	−117.4715	34.1359	13.33	3.53	315	86	177	73%	
9163314	−118.421	33.9868	10.35	3.08	264	48	82	54%	
9164156	−117.7381	34.1587	9.82	3.01	62	81	−2	54%	
9520538	−117.4793	34.1828	3.28	3.14	311	68	175	98%	
9639729	−117.5806	34.0349	9.91	3.35	325	86	−174	95%	

Figure 2. CMT solutions with fault-plane ambiguity resolutions for the earthquakes studied in this paper. Column 1, the event ID number, which is unique for each earthquake in Southern California Seismic Network (SCSN) catalogue; columns 2–4, longitude, latitude and depth of events' centroid locations; column 5, local magnitude; columns 6–8, strike, dip, and rake of the best-fit-double-couple (bfdc) solutions; column 9, likelihood of the picked nodal plane to be the actual fault plane based on a Bootstrap procedure; column 10, beachball plots of the bfdc solutions with the preferred fault planes highlighted in black thick lines.

Here $I_x(\omega, \omega_n)$ is a bell-shaped function centred around ω_n with its width controlled by the windowing and filtering parameters chosen during the GSDF processing (Chen 2005 chapter 2; Chen *et al.* 2007a).

In this study, only amplitude-reduction time $\delta t_q(\omega_n)$ were used to distinguish the two nodal planes of the CMT solution. For the frequency range used in this study, we found that the sensitivity of δt_q with respect to the directivity effect $\mu^{(1,1)}$ is only about one tenth of the sensitivity with respect to the source finiteness $\mu^{(2,0)}$ (Chen *et al.* 2005); therefore we ignore the contributions from $\mu^{(1,1)}$ in calculating the model-predicted $\delta\tilde{\tau}_q$. In our automated procedure, we first estimate the rupture dimension from the scalar moment; then calculate the model-predicted $\delta\tilde{t}_q(\omega_n)$ using eqs (8a) and (10). The correlation coefficient between the actual measurements δt_q^l and model predictions $\delta\tilde{t}_q^l$ are calculated as

$$C = \frac{\sum_{l=1}^{n}\left[\delta\tilde{t}_q^l - E\left(\delta\tilde{t}_q^l\right)\right]\left[\delta t_q^l - E\left(\delta t_q^l\right)\right]}{(n-1)std\left(\delta\tilde{t}_q^l\right)std\left(\delta t_q^l\right)}. \quad (11)$$

Here $E()$ denotes the mean and $std()$ denotes the standard deviation, l is the index for measurements made at different azimuth θ, frequency ω, distance r and component k, n is the total number of measurements used to calculate the correlation coefficient C. The nodal plane that provides a higher correlation coefficient is identified as the actual fault plane by our automated procedure.

To quantify the likelihood that the automatically picked nodal plane is the actual fault plane, we adopted a bootstrap method. In each iteration of our bootstrap process, we randomly select half of our measurements and compute the correlation coefficients for the two conjugate nodal planes of our CMT solution using eq. (11). The nodal plane that provides a larger correlation coefficient for more than half of our bootstrap iterations is identified as the actual fault plane. The likelihood that the picked fault plane is the real fault plane is computed as the ratio between the number of bootstrap iterations for which the pick fault plane provides a larger correlation coefficient and the total number of bootstrap iterations.

RESULTS

The geographic area of our study is shown in Fig. 1. We constructed a RGT database for the 48 CISN stations located in this area using the finite-difference method. The calculated RGTs are accurate up to 1 Hz. Synthetic seismograms at these 48 stations from an arbitrary point source located in our modelling volume can be easily computed by retrieving a small source-centred volume from our RGT database and calculating the source-coordinate gradient (eq. 1). At the same time, we also calculate the partial derivatives needed for CMT inversion (Zhao *et al.* 2006) and the higher-order gradients in eq. (8) needed for testing the two nodal planes of our CMT solution.

The fault planes picked by our automated procedure as well as the likelihood computed from 1000 bootstrap iterations are shown in Figs 1 and 2. In general, the likelihood calculated from the bootstrap method is higher for earthquakes with good receiver coverage. In Fig. 3, we show the distributions of the differences between the correlation coefficients calculated for the two nodal planes as well as the azimuthal coverage of the receivers used to resolve fault plane ambiguity for three earthquakes: the 2002 September 3 M 4.8 Yorba Linda earthquake, the 2001 September 9 M4.2 Hollywood earthquake, and the 2005 January 6 M4.4 Fontana earthquake. For these three events and several other smaller events, the fault planes picked by our automated procedure were confirmed by the distributions of relocated aftershock hypocentres (Fig. 3c). The Yorba Linda earthquake, which has the best receiver coverage among the three earthquakes, also has the highest likelihood computed from the bootstrap method, while the Fontana earthquake, which has the

Event ID	Longitude	Latitude	Depth	Mag	Strike	Dip	Rake	Likelihood	Beachball
9644101	−117.7027	33.8724	1.86	3.64	328	86	180	91%	
9652545	−117.4418	34.2199	9.89	3.84	314	85	−177	70%	
9659437	−117.4672	34.2213	13.03	3.16	301	62	137	51%	
9703873	−118.3842	34.0585	8.02	4.24	138	79	160	85%	
9706897	−117.7846	33.9227	9.26	3.1	43	82	−1	89%	
9716853	−118.2743	33.9269	19.39	3.98	314	76	−164	88%	
9735129	−117.7442	33.9532	12.28	3.97	215	90	20	79%	
9808837	−117.4389	34.1604	8.96	3.04	156	73	−161	89%	
9818433	−117.7811	33.918	9.47	4.75	30	90	0	97%	
9923613	−117.4742	34.1773	4.0	3.38	165	81	−89	92%	
9970349	−117.8152	33.9705	16.74	3.53	231	71	0	99%	
9970365	−117.8155	33.9733	16.33	3.18	229	73	14	94%	
9981381	−117.5082	33.733	7.19	3.01	60	49	48	75%	

Figure 2. (*Continued.*)

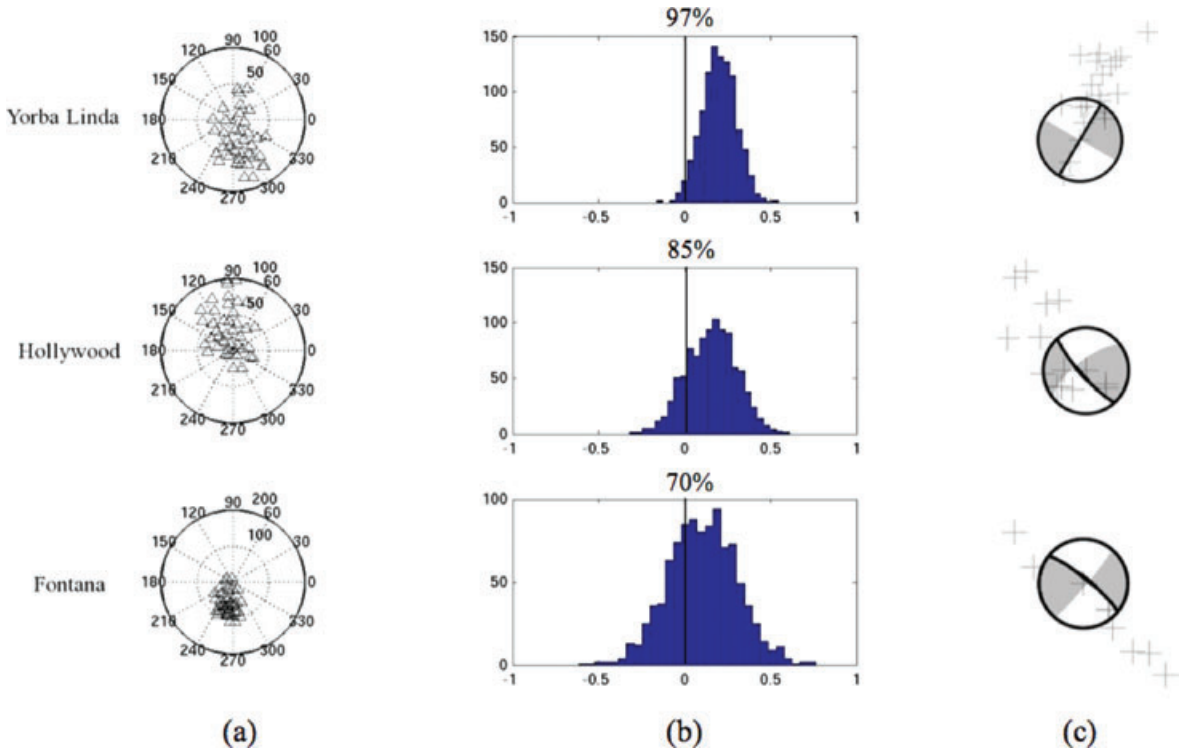

Figure 3. (a) Triangles show azimuthal distributions of receivers used in resolving fault-plane ambiguity, 0° correspond to North; (b) distributions of correlation–coefficient differences calculated for the two nodal planes of our CMT solutions for three earthquakes, the numbers on top of the panels are the percentages of the number of iterations lying on the positive side; (c) crosses show distributions of aftershock epicentres as relocated by the authors using *hypoDD* (Waldhauser & Ellsworth 2000).

worst receiver coverage among the three earthquakes, has the lowest likelihood.

Among the 35 earthquakes that we have resolved fault-plane ambiguity for, there are two clusters. One is the 'Fontana trend' (Hadley & Combs 1974; Cramer & Harrington 1987; Sheridan 1997; Plesch *et al.* 2003) located to the southwest of the right-lateral San Jacinto fault and the north-dipping Cucamonga fault (Figs 1 and 4). The Fontana trend is not associated with any mapped surface fault traces (Plesch *et al.* 2003). The other seismicity anomaly is the 'Yorba Linda cluster' (Walls *et al.* 1998; Plesch *et al.* 2003; Chen *et al.* 2005) located about 20 miles to the southwest of the 'Fontana trend' and near the right-lateral Whittier fault. The CMT solutions for the earthquakes in the Fontana trend are similar to those in the Yorba Linda cluster (Fig. 1), but the fault planes picked by our automated procedure show that the earthquakes in these two clusters have very different source mechanisms (Figs 1 and 4). Most of the earthquakes in the Yorba Linda cluster show left-lateral faulting conjugate to the nearby right lateral Whittier fault, while the earthquakes in the Fontana trend show right-lateral faulting parallel to the San Jacinto fault (Fig. 4). The underlying causes for these two anomalous clusters are still under investigation, but this example demonstrates that our new technique are potentially useful for providing additional constraints to regional tectonics.

DISCUSSION

The methodology discussed in this paper is generally applicable. It does not rely on detecting the directivity effect; therefore it can be applied to any seismic sources including bilateral earthquakes with zero directivity. In regions where there are no precisely relocated aftershocks or for earthquakes with few aftershocks, we expect our methodology to be the most convenient means for resolving fault-plane ambiguity.

By removing fault-plane ambiguities from CMT solutions in a routine manner, we can provide clearer pictures on regional tectonics. Resolving fault-plane ambiguity from CMT solutions can also reduce the uncertainties in regional stress inversions based on earthquake focal mechanism data (Gephart 1985; Michael 1987; Gephart 1990; Yin 1996). The identified fault planes can also be used in calculating Coulomb stress changes and provide a more robust description of probabilistic seismic hazard based on the stress transfer model (Harris 1998; McCloskey *et al.* 2003; Parsons 2005; Steacy *et al.* 2005).

This automated procedure for picking the fault plane from the two conjugate nodal planes of our CMT solutions is a generic module of our computational framework for unified seismic data processing. The same types of GSDF measurements used to improve our seismic source models were also used to refine our seismic structure models iteratively in linearized tomographic inversions (Chen *et al.* 2007a). The RGT database used in our seismic source inversion procedures were also used to compute the sensitivity kernels of the GSDF measurements with respect to the seismic structure model using the scattering-integral method (Zhao *et al.* 2005; Chen *et al.* 2007b). We expect this unified seismic data processing framework, which is based on the GSDF measurements and RGT database, will provide seismologists a general platform for seismic waveform analysis and inversion at different geographic scales.

ACKNOWLEDGMENTS

This research was supported by the Southern California Earthquake Center; SCEC is funded by NSF Cooperative Agreement

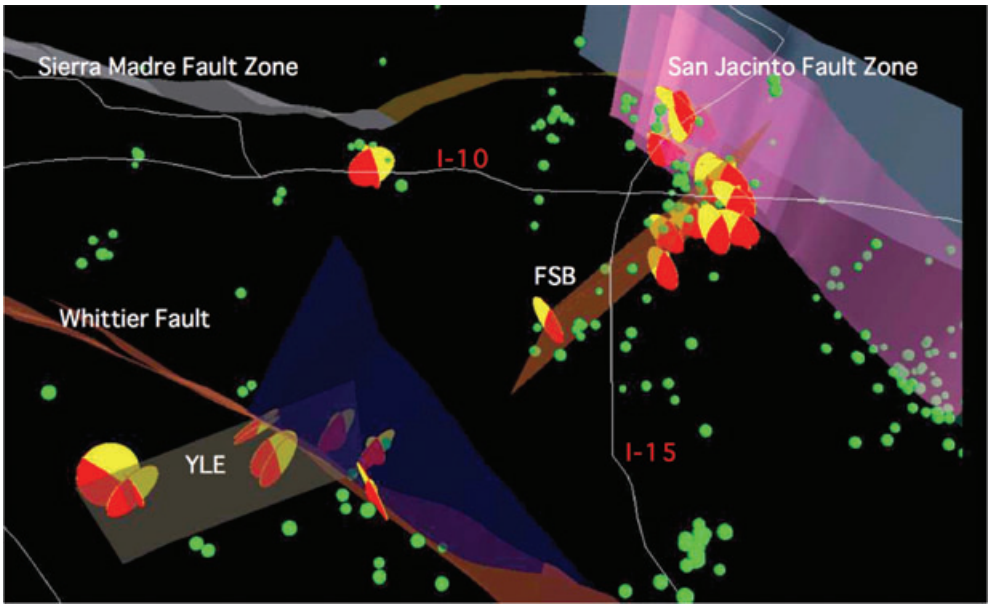

Figure 4. Projection of a 3-D rendering of the focal mechanisms for earthquakes in the Yorba Linda cluster and the Fontana trend (Fig. 1). Focal mechanisms are represented as two intersecting disks, whose sizes are proportional to the likelihood of being the actual fault plane as determined in this study. Extensive quadrants are painted in yellow and compressive quadrants are painted in red. Major faults in this area are represented as coloured transparent surfaces. The surfaces denoted as 'Fontana Seismicity Bestfit' (FSB) and 'Yorba Linda Extruded' (YLE) are linear least-square fit to the hypocentres of the earthquakes in the Fontana trend and the Yorba Linda cluster, respectively. Locations and orientations of the faults as well as the FSB and YLE surfaces are obtained from the SCEC Community Fault Model (CFM-A). Background seismicity is shown as green spheres. Major highways in this area are plotted as white solid lines and the interstate freeways I-10 and I-15 are labelled in red. The 3-D rendering was done using the Java3D-based interactive 4-D visualization software SCEC-VDO (http://scecdata.usc.edu/scecinterns/index.php?title=UseIT:_SCEC-VDO_User%27s_Page) developed by the SCEC Undergraduate Studies in Earthquake Information Technology (UseIT) interns under the supervision of Sue Perry (perry@usc.edu).

EAR-0106924 and USGS Cooperative Agreement 02HQAG0008. High-throughput computations were supported by the SCEC Community Modeling Environment under NSF grant EAR-0122464 and the University of Southern California Center for High Performance Computing and Communications; we thank P. Maechling and other members of CME collaboration and G. Staples from USC/HPCC for help in implementing the simulation and inversion algorithms. Comments from Prof J. Zahradnik and an anonymous reviewer improved the manuscript.

REFERENCES

Akçelik, V. *et al*., 2003. High resolution forward and inverse earthquake modeling on terasacale computers, in *Proceedings of the ACM/IEEE SC2003 Conference,* Phoenix, Arizona.

Aki, K. & Richards, P.G., 2002. *Quantitative Seismology,* 2nd edn, University Science Books, Sausalito, CA.

Backus, G. & Mulcahy, M., 1976. Moment tensors and other phenomenological descriptions of seismic sources, I. Continuous displacements, *Geophys. J. R. astr. Soc.,* **46,** 341–361.

Bao, H., Bielak, J., Ghattas, O., Kallivokas, L.F., O'Hallaron, D.R., Shewchuk, J.R. & Xu, J., 1998. Large-scale simulation of elastic wave propagation in heterogeneous media on parallel computers, *Comput. Methods Appl. Mech. Engrg.,* **152,** 85–102.

Ben-Menahem, A., 1961. Radiation of seismic surface-waves from moving sources, *Bull. seism. Soc. Am.,* **51,** 403–435.

Chen, P., 2005. A Unified methodology for seismic waveform analysis and inversion, *PhD dissertation*, University of Southern California (http://www-rcf.usc.edu/~pochen/index.html).

Chen, P., Zhao, L. & Jordan, T.H., 2005. Finite moment tensor of the 3 September 2002 Yorba Linda Earthquake, *Bull. seism. Soc. Am.,* **95**(3), 1170–1180.

Chen, P., Zhao, L. & Jordan, T.H., 2007a. Full 3D tomography for crustal structure in the Los Angeles region, *Bull. seism. Soc. Am.,* **97**(4), 1094–1120.

Chen, P., Jordan, T.H. & Zhao, L., 2007b. Full 3D Tomography: a comparison between the scattering-integral and adjoint-wavefield methods, *Geophys. J. Int.,* **170,** 175–181. doi:10.1111/j.1365-246X.2007.03429.x

Cramer, C.H. & Harrington, J.M., 1987. Seismicity and tectonics of the Cucamonga fault and the eastern San Gabriel Mountains, San Bernardino County, in *Recent reverse faulting in the Transverse Ranges,* California, U. S. Geol. Surv. Profess. Paper 1339, 7–26.

Dahlen, F.A. & Tromp, J., 1998. *Theoretical Global Seismology,* Princeton University Press, Princeton, NJ, 1025 pp.

Gee, L.S. & Jordan, T.H., 1992. Generalized Seismological data functionals, *Geophys. J. Int.,* **111,** 363–390.

Gephart, J.W., 1985. Principal stress directions and the ambiguity in fault plane identification from focal mechanism, *Bull. seism. Soc. Am.,* **75,** 621–625.

Gephart, J.W., 1990. Stress and the direction of slip on fault planes, *Tectonics,* **9,** 845–858.

Graves, R.W., 1996. Simulating seismic wave propagation in 3D elastic media using staggered-grid finite differences, *Bull. seism. Soc. Am.,* **86,** 1091–1106.

Hadley, D. & Combs, J., 1974. Microearthquake distribution and mechanisms of faulting in the Fontana-San Bernardino area of Southern California, *Bull. seism. Soc. Am.,* **64**(5), 1477–1499.

Harris, R.A., 1998. Introduction to special session: stress triggers, stress shadows, and implications for seismic hazard, *J. geophys. Res.,* **103,** 24 347–24 358.

Hellweg, M. & Boatwright, J., 1999. Mapping the rupture process of moderate earthquakes by inverting accelerograms, *J. geophys. Res.,* **104,** 7319–7328.

Kohler, M.D., Magistrale, H., Clayton, R.W., 2003. Mantle heterogeneities and the SCEC reference three-dimensional seismic velocity model version 3, *Bull. seism. Soc. Am.,* **93,** 757–774.

Komatitsch, D., Liu, Q., Tromp, J., Süss, P., Stidham, C. & Shaw, J.H., 2004. Simulations of ground motion in the Los Angeles basin based upon spectral-element method, *Bull. seism. Soc. Am.,* **94,** 187–206.

Magistrale, H., Day, S., Clayton, R.W. & Graves, R., 2000. The SCEC Southern California Reference Three-dimensional Seismic Velocity Model Version 2, *Bull. seism. Soc. Am.,* **90,** S65–S76.

McCloskey, J., Nalbant, S.S., Steacy, S., Nostro, C., Scotti, O. & Baumont, D., 2003. Structural constraints on the spatial distribution of aftershocks, *Geophys. Res. Lett.,* **30**(12), 1610, doi:10.1029/2003GL017225.

McGuire, J., 2004. Estimating finite source properties of small earthquake ruptures, *Bull. seism. Soc. Am.,* **94**(2), 377–393.

McGuire, J.J., Zhao, L., & Jordan, T.H., 2001. Teleseismic inversion for the second-degree moments of earthquakes, *Geophys. J. Int.,* **145,** 661–678.

McGuire, J.J., Zhao, L. & Jordan, T.H., 2002. Predominance of unilateral rupture for a global catalog of large earthquakes, *Bull. seism. Soc. Am.,* **92**(8), 3309–3317.

Michael, A.J., 1987. Use of focal mechanisms to determine stress: a control study, *J. geophys. Res.,* **92,** 357–368.

Mori, J., 1996. Rupture directivity and slip distribution of the M 4.3 foreshock to the 1992 Joshua Tree earthquake, Southern California, *Bull. seism. Soc. Am.,* **86,** 805–810.

Mori, J. & Hartzell, S., 1990. Source inversion of the 1988 upland, California, earthquake: determination of a fault plane for a small event, *Bull. seism. Soc. Am.,* **80,** 507–518.

Okada, T., Umino, N., Ito, Y., Matsuzawa, T., Hasegawa, A. & Kamiyama, M., 2001. Source processes of 15 September 1998 M5.0 Sendai, Northeastern Japan, Earthquake and Its M3.8 foreshock by waveform inversion, *Bull. seism. Soc. Am.,* **91,** 1607–1618.

Olsen, K.B., 1994. Simulation of three-dimensional wave propagation in the Salt Lake Basin, *PhD thesis*. University of Utah, Salt Lake City, Utah, 157p.

Olsen, K.B. *et al*., 2006. Strong shaking in Los Angeles expected from southern San Andreas earthquake, *Geophys. Res. Lett.,* **33,** L07305, doi:10.1029/2005GL025472.

Olsen, K.B., Day, S.M. & Bradley, C.R., 2003. Estimation of Q for long-period (>2 s) waves in the Los Angeles Basin, *Bull. seism. Soc. Am.,* **93,** 627–638.

Parsons, T., 2005. Significance of stress transfer in time-dependent earthquake probability calculations, *J. geophys. Res.,* **110,** B05S02, doi:10.1029/2004JB003190.

Plesch, A., Shaw, J.H. & SCEC CFM Working Group, 2003. SCEC CFM—a WWW accessible community fault model for Southern California, *EOS, Trans. Am. geophys. Un.,* **84,** S12B–0395.

Press, W.H., Teukolsky, S.A., Vetterling, W.T. & Flannery, B.R., 1992. *Numerical Recipes in C—The Art of Scientific Computing,* Cambridge University Press, New York, NY.

Sato, T. & Hirasawa, T., 1973. Body wave spectra from propagating shear cracks, *J. Phys. Earth,* **21,** 415–431.

Sheridan, J.M., 1997. Secondary deformation near strike-slip faults, Southern California, *PhD thesis*. Eugene, University of Oregon, 253 pp.

Silver, P. & Jordan, T.H., 1983. Total-moment spectra of fourteen large earthquakes, *J. geophys. Res.,* **88,** 3273–3293.

Steacy, S., Nalbant, S.S., McCloskey, J., Nostro, C., Scotti, O. & Baumont, D., 2005. Onto what planes should Coulomb stress perturbations be resolved? *J. geophys. Res.,* **110,** B05S15, doi:10.1029/2004JB003356.

Süss, M.P. & Shaw, J.H., 2003. P-wave seismic velocity structure derived from sonic logs and industry reflection data in the Los Angeles basin, California, *J. geophys. Res.,* **108**(B3), 2170, ESE 13.

Waldhauser, F. & Ellsworth, W.L., 2000. A double-difference earthquake location algorithm: method and application to the northern Hayward fault, California, *Bull. seism. Soc. Am.,* **90,** 1353–1368.

Walls, C., Rockwell, T., Mueller, K., Bock, Y., Williams, S., Pfanner, J., Dolan, J. & Feng, P., 1998. Escape tectonics in the Los Angeles metropolitan region and implications for seismic risk, *Nature,* **394,** 356–360.

Yin, Z.-M., 1996. An improved method for the determination of the tectonic stress field from focal mechanism data, *Geophys. J. Int.,* **125,** 841–849.

Zhao, L., Jordan, T.H., Olsen, K.B. & Chen, P., 2005. Fréchet kernels for imaging regional Earth structure based on three-dimensional reference models, *Bull. seism. Soc. Am.,* **95**(6), 2066–2080.

Zhao, L., Chen, P. & Jordan, T.H., 2006. Strain Green's tensors, reciprocity and their applications to seismic source and structure studies, *Bull. seism. Soc. Am.,* **96**(5), 1753–1763.

APPENDIX

We consider a circular crack with symmetric slip distribution and the slip rate on the fault plane is (Sato & Hirasawa 1973)

$$\Delta v(r_S, t) = \frac{24\Delta\sigma}{7\pi\mu}\frac{V^2 t}{\sqrt{(Vt)^2 - r_S^2}} H(Vt - r_S)H(R - Vt). \quad \text{(A1)}$$

Here, $\Delta\sigma$ is stress-drop, μ is the shear modulus in the source region, V is the rupture propagation velocity, R is the final radius of the circular crack and $H(t)$ is the Heaviside function.

The scalar moment for such a kinematic source model is $M_0 = (16/7)\,\Delta\sigma R^3$. We set up our coordinate system as shown in Fig. A1, we have the centroid location $\boldsymbol{\mu}^{(1,0)} = 0$ and the centroid time $\mu^{(0,1)} = (3/4)R/V$. The mixed space–time moment that accounts for the directivity effect is exactly zero $\boldsymbol{\mu}^{(1,1)} = 0$ for such a symmetric source. The second-order temporal moment is $\mu^{(0,2)} = (3/5)\,(R/V)^2$. The second-order spatial moment is $\boldsymbol{\mu}^{(2,0)} = (R^2/5)$ diag[1, 0, 1], if the rupture lies in the x–z plane, and $\boldsymbol{\mu}^{(2,0)} = (R^2/5)$ diag[0, 1, 1], if the rupture lies in the y–z plane. Here diag[] denotes a diagonal matrix.

To simplify discussion, we consider the far-field term in the whole-space Green's function (Aki & Richards 2002)

$$\tilde{u}(\mathbf{r}, \omega) = \frac{P(\theta, \phi)}{4\pi\rho c^3 r}\exp(\mathrm{i}\omega r/c), \quad \text{(A2)}$$

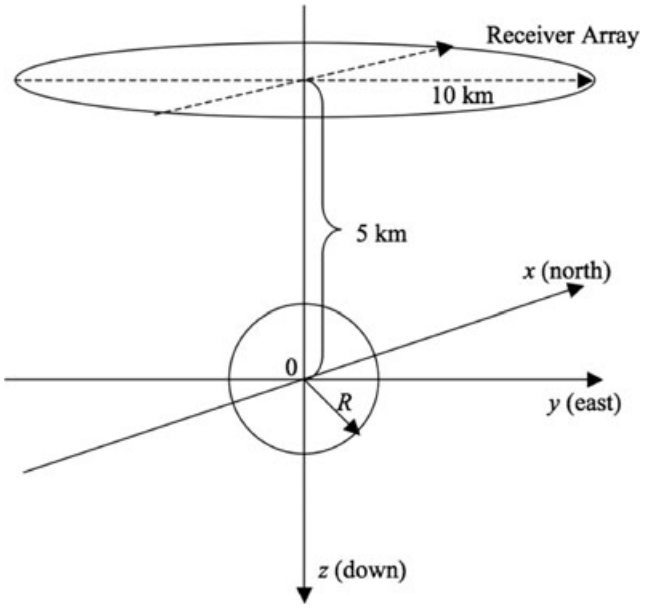

Figure A1. Source–receiver configuration for the numerical experiments given in the Appendix. We consider two circular cracks, one lies in the x–z plane, the other lies in the y–z plane. The one lying in the x–z plane is not shown here. The radius of the circular cracks is 1 km, rupture propagation velocity is 2 km s^{-1}. The receiver array is circular, with radius 10 km and lies 5 km above the source. The shear modulus in the source region is 300 kbar and stress drop is 30 bars.

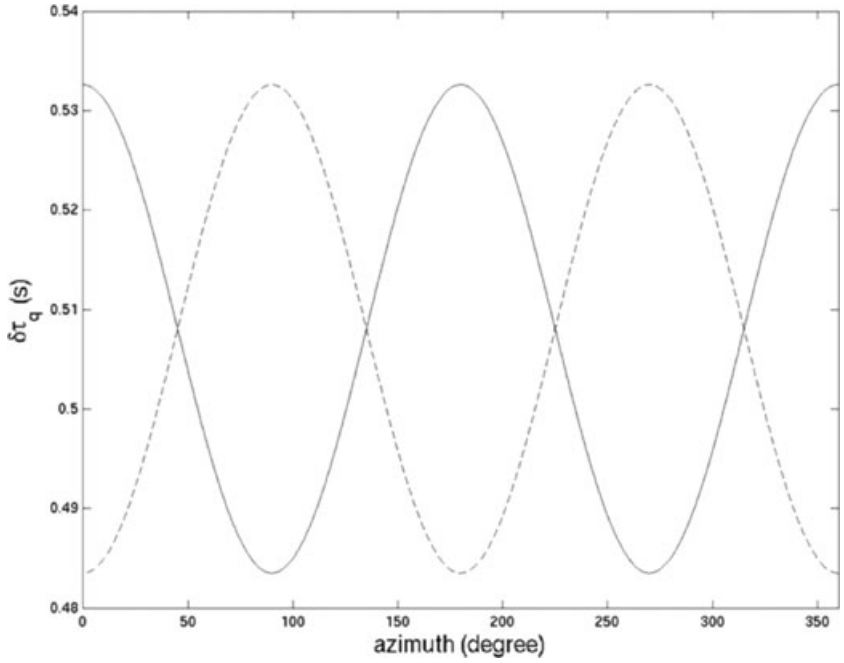

Figure A2. The azimuthal variations of $\delta\tilde{\tau}_{\rm q}$ at 1.0 Hz for the circular crack lying in the *x*–*z* plane (solid line) and the one lying in the *y*–*z* plane (dash line). Shear waves on the transverse components are used. Shear wave velocity is 3.2 km s^{-1}. Source–receiver configuration is shown in Fig. A1. The whole-space Green's function is used to calculate point-source synthetics and the partial derivatives.

where, c is *P*- or *S*-wave speed, ρ is density, $\mathbf{r} = \mathbf{r}_{\rm R} - \mathbf{r}_{\rm S} = r\hat{\mathbf{r}}$ and $P(\theta, \phi)$ denotes the radiation pattern. If we bring eq. (A2) into eq (8), use spherical decomposition $\nabla = \hat{\mathbf{r}}\partial_r + \nabla_1/r$ (Dahlen & Tromp 1998), for the circular crack source model, we obtain

$$\delta\tilde{\tau}_{\rm q}(\mathbf{r}, \omega) = \frac{\omega}{2}\mu^{(0,2)} + \frac{\omega}{2c^2}\hat{\mathbf{r}} \cdot \boldsymbol{\mu}^{(2,0)} \cdot \hat{\mathbf{r}} - \frac{\boldsymbol{\mu}^{(2,0)}}{2\omega r^2} : \frac{\nabla_1\nabla_1 P}{P}, \qquad \text{(A3)}$$

$$\delta\tilde{\tau}_{\rm p}(\mathbf{r}, \omega) = \mu^{(0,1)} + \frac{1}{cr}\hat{\mathbf{r}} \cdot \boldsymbol{\mu}^{(2,0)} \cdot \frac{\nabla_1 P}{P}. \qquad \text{(A4)}$$

If we bring the FMTs into eq. (A3), for the source–receiver configuration shown in Fig. (A1), the model predicted azimuthal variations of $\delta\tilde{\tau}_{\rm q}$ are shown as the solid line for a rupture lies in the *x*–*z* plane and as the dash line for a rupture lies in the *y*–*z* plane (Fig. A2). Since the contributions from $\boldsymbol{\mu}^{(1,0)}$ and $\boldsymbol{\mu}^{(1,1)}$ are zero and contributions from $\mu^{(0,1)}$ and $\mu^{(0,2)}$ do not have azimuthal dependence, the azimuthal variation of model predicted $\delta\tilde{\tau}_{\rm q}$ is caused by the second-order spatial moment $\boldsymbol{\mu}^{(2,0)}$ only. As shown in Fig. A2, the contribution from $\boldsymbol{\mu}^{(2,0)}$ has a $\cos(2\theta)$-dependence on azimuth. If the rupture lies in the *x*–*z* plane, $\delta\tilde{\tau}_{\rm q}$ has two minima (i.e. maxima in waveform amplitude) at 0° and 180°, which is caused by constructive interference from different points on this circular source, and two maxima (i.e. minima in waveform amplitude) at 90° and 270°, which is caused by destructive interference. For a rupture lies in the *y*–*z* plane, the minima are at 90° and 270°, while the maxima are at 0° and 180°.

For a fixed receiver location, $\delta\tilde{\tau}_{\rm q}$ also has different frequency-dependences for the two ruptures lying in the *x*–*z* and *y*–*z* planes as shown in eq. (A3).

An important issue in detecting second-order source effects is the signal-to-noise ratio. The contribution to $\delta\tilde{\tau}_{\rm q}$ from the second-order spatial moment $\mu^{(2,0)}$ is

$$\left\| \frac{\tilde{\mathbf{X}}}{2} : \boldsymbol{\mu}^{(2,0)} \right\| \leq \frac{\omega}{10}\left(\frac{R}{c}\right)^2 + \frac{1}{10\omega}\left(\frac{R}{r}\right)^2. \qquad \text{(A5)}$$

The first term on the right-hand side of eq. (A5) does not depend on source–receiver distance; therefore, it is possible to detect the contribution from $\boldsymbol{\mu}^{(2,0)}$ in the far field when the frequency is sufficiently high. For shear wave speed $\beta \sim V$, this term is roughly one third of the contribution from $\mu^{(0,2)}$. The second term on the right-hand side of eq. (A5) is significant in the near field and increases as we decrease frequency. For local small to medium-sized earthquakes ($2.5 \leq M_{\rm L} \leq 5$), we found that the contribution from $\boldsymbol{\mu}^{(2,0)}$ is statistically significant for source–receiver distance ranging from 10 to 50 km and for frequency ranging from 0.1 to 0.5 Hz.